Energy Advances

PAPER

View Article Online
View Journal | View Issue

Cite this: *Energy Adv.*, 2024, 3, 2947

Evaluation of the electrochemical energy storage performance of symmetric supercapacitor devices based on eco-friendly synthesized nitrogen-doped graphene-like derivative electrodes from the perspective of their nanostructural characteristics†

Marwa A. A. Mohamed, *[a] Marwa Adel [ab] and Jehan El Nady [c]

The potential use of several ecofriendly nitrogen-doped 2D graphene-like derivatives (N-2D GDs) with various graphitic structural features as electrode materials for symmetric 2-electrode supercapacitor devices was explored. The N-2D GDs were synthesized *via* a novel, facile, ecofriendly, economic and scalable technique. The synthesis technique is simply a single-step hydrothermal treatment of glucose using traces of cetyltrimethylammonium bromide (CTAB) and ammonia as structure-directing agents. Graphitic structural characteristics were controlled by manipulating hydrothermal process temperature and CTAB dose. Electrochemical energy storage performance was found to be strongly dependent on the oxidation level, doped-N content and configuration, density of graphitic surface-capping by CTAB, morphological architecture and graphitic structural order of N-2D GD-based electrodes. Interestingly, such graphitic structural parameters influenced overall charge-storage capacitance through EDLC and pseudocapacitance mechanisms in a competitive manner. An N-2D GD sample synthesized at a hydrothermal temperature of 270 °C and CTAB/glucose molar ratio of 1/6 (NG-HCD270) exhibited the best energy storage capacitive performance in a symmetric 2-electrode supercapacitor system owing to the almost pure well-ordered N-doped graphene. It showed excellent electrochemical energy storage performance as compared to other 2D graphene derivatives reported in the literature synthesized *via* toxic conventional methods, with a specific capacitance of 553 F g^{-1}, energy density of 84.5 W h kg^{-1}, power density of 550.2 W kg^{-1} and 88.5% capacitance retention after 5000 cycles. Thus, the NG-HCD270 graphitic sample can be considered a promising ecofriendly and cost-effective electrode material for high-performance supercapacitors, which can benefit the substantial development of electrical energy storage industry and, hence, electrical power production from renewable energy sources at competitive costs.

Received 5th September 2024,
Accepted 17th October 2024

DOI: 10.1039/d4ya00526k

rsc.li/energy-advances

1. Introduction

The looming global energy crisis and urgent worldwide demand for a clean and healthy environment call for clean, lasting and cost-effective energy sources as replacements for fossil fuels. In this regard, renewable and sustainable energy sources based on solar, wind, hydropower, bio-based fuel, geothermal power and hydrogen have attracted worldwide attention. Continuous innovation in technologies related to electrical power supply from renewable energy sources, specifically generation, storage, and delivery, is essential to meet worldwide challenges for greater reliance on renewable energy sources for fulfilling the global electricity demand.[1,2] Supercapacitors, with higher electrical energy density than traditional capacitors and higher electrical power density,

[a] *Fabrication Technology Department, Advanced Technology and New Materials Research Institute, City of Scientific Research and Technological Applications (SRTA City), New Borg El-Arab 21934, Alexandria, Egypt.*
E-mail: mmohamed@srtacity.sci.eg, marwa945@yahoo.com; Fax: +2-03-4593414; Tel: +2-03-4600257
[b] *Petroleum Applications Department, Egyptian Petroleum Research Institute (EPRI), Nasr City 11727, Cairo, Egypt*
[c] *Electronic Materials Department, Advanced Technology and New Materials Research Institute, City of Scientific Research and Technological Applications (SRTA City), New Borg El-Arab 21934, Alexandria, Egypt*

† Electronic supplementary information (ESI) available: XPS elemental analysis and Raman spectra of all investigated graphitic samples. Further SEM micrographs of the NG-HCD250 & NG-HCD270 graphitic samples and HR-TEM images of the NG-HCD270 graphitic sample. See DOI: https://doi.org/10.1039/d4ya00526k

longer cycling life and lower maintenance cost than batteries, are at the forefront of present-day electrochemical energy storage systems. They have been successfully applied in electric vehicles, portable electronic devices and several emergency power supply devices.[3–5] However, substantial enhancement of supercapacitors' energy density is required to meet higher power requirements of large industrial equipment and main electric grids and thereby to broaden their application areas.[5,6] In this regard, the electrode material of supercapacitors is critical. Based on the energy storage mechanism, supercapacitors can store energy through either an electrochemical double-layer capacitance (EDLC) mechanism or pseudocapacitance mechanism, in addition to their hybrid combinations. In EDLC, energy storage is achieved through the accumulation of charges at electrode–electrolyte interfaces, where electrodes are usually made of carbon-based materials. Alternatively, charge storage is realized *via* the pseudocapacitance mechanism through redox faradaic reactions, where transition metal oxides and conductive polymers are the most widely used electrode materials.[5]

Graphene is a one-atom thick sheet of uniformly organized sp^2 bonded carbon atoms in a hexagonal crystalline lattice. The unique two-dimensional (2D) planar nanostructure of graphene affords it many superb physicochemical properties. So, 2D graphene derivatives have been widely considered as leading candidate materials for substantial advancements in various technological industries, such as energy, electronics, sensors, catalysis, environmental remediation, biomedical, and structural sectors. In particular, with an extensively large specific surface area ($\sim 2630\ m^2\ g^{-1}$), exceptional electrical conductivity ($\sim 1.5 \times 10^6\ S\ m^{-1}$), extraordinary mechanical durability (Young's modulus ~ 1 TPa and ultimate strength ~ 130 GPa) and high chemical stability, graphene is one of the most promising EDLC electrode materials for supercapacitors.[4,7]

The chemical doping of graphene by heteroatoms, such as nitrogen, boron, phosphorus, hydrogen *etc.*, leads to the disruption of the sp^2 hybridization of carbon atoms in the hexagonal lattice, which results in significant changes in graphene's physical and chemical properties. Nitrogen (N) has been the most widely applied heteroatom in the chemical doping of graphene. There are predominantly four different bonding configurations for the embedded N atoms in the carbon lattice: graphitic (quaternary) N, pyridinic N, pyrrolic N, and oxidized N (NO_x).[4,8,9] Many research groups have reported a positive effect of N-doping on the capacitance enhancement of graphene-based electrodes and consequently an increase in the energy density in the whole supercapacitor system.[4] It is believed that the N-doping of graphene enhances the supercapacitor's electrode capacitance behavior mainly because it causes considerable changes in graphene's electronic structure, which leads to several effects: (a) it increases the charge carrier density, which results in fast electron transfer and, consequently, increased intrinsic electrical conductivity, which enhances the capacitance by the EDLC mechanism,[4,10] (b) it increases the concentration of hydrophilic polar sites on the electrode surface in aqueous electrolytes, leading to improved electrode wettability and a higher EDLC capacitance in aqueous electrolytes,[4,11] (c) it induces a pseudocapacitive contribution in aqueous electrolytes. Here, doped-N functionalities are usually either located on the edge or on a defect site of the graphene basal plane, initiating redox faradaic conversions with ions in acidic and alkaline electrolytes, which suggests that the pseudocapacitance mechanism is a potential strategy for improving the capacitance of N-doped graphene-based electrodes in aqueous electrolytes, compared to pristine graphene-based electrodes.[4,12,13]

The industrial-scale mass production of N-doped 2D graphene derivatives (N-2D GDs) was focused on in this study, to enable their commercial exploitation in technological applications. In this regard, the most commonly used techniques for the large-scale production of 2D GDs are the oxidative-reduction, liquid-phase exfoliation, chemical-vapor deposition (CVD), and total organic synthesis approaches. However, the conventional strategies employed through such techniques for the synthesis of GD nanosheets typically involve the utilization of hazardous and toxic chemicals, which can cause serious human health problems and environmentally harmful effects. Alternatively, in recent years, green synthetic protocols using ecofriendly reagents for the large-scale production of 2D GDs have been strongly encouraged all over the world, in order to alleviate the problems of industrial pollution.[14–16]

Recently, we synthesized N-2D GDs *via* a novel, facile, ecofriendly, cost-effective, and scalable technique involving a one-pot single-step process; namely a simple hydrothermal treatment of glucose under mild conditions, utilizing small concentrations of cetyltrimethylammonium bromide (CTAB) and ammonia solution (NH_4OH) as structure-directing agents. The hydrothermal temperature and CTAB dose were manipulated and N-2D GDs with various structural features were obtained. The products ranged from N-doped oxidized graphitic carbon with a mixed micro-sized sphere/sheet morphology to highly reduced N-doped graphene-like nanosheets.[8] The present research explored the potential use of such ecofriendly developed N-2D GDs as supercapacitor electrodes. The research aimed to understanding how the characteristic graphitic nanostructured features could impact and control the electrochemical capacitive performances of symmetric 2-electrode supercapacitor devices based on the investigated N-2D GDs electrodes. The best electrochemical capacitive performance in the present study was compared to those reported in the literature for graphene-like nanosheets produced by conventional technologies (such as graphite oxidation–reduction, graphite liquid-phase exfoliation) for evaluation purposes. Thus, the present study can make a significant contribution to the ecofriendly and economical manufacture of high-grade N-2D GDs-based electrodes for supercapacitor applications.

2. Experimental

2.1. Materials

The key chemicals used for synthesis of the N-2D GDs comprised anhydrous crystalline D-glucose (99.5%) as the carbon

precursor, and cetyltrimethylammonium bromide (CTAB, 99.5%) and ammonium hydroxide (NH_4OH, 33% NH_3) as graphitic structure-directing agents. They were purchased from Cargill, Egypt, WINLAB, UK, and Sigma-Aldrich, Europe, respectively. Doubly distilled water was the aqueous medium employed throughout the synthesis processes. For the electrodes fabrication, polyvinylidinefloride (PVDF, 98%), carbon black (99+%), and 1-methyl 2-pyrrolidinone (99+%) were utilized, as procured from Alfa Aesar. Nickel sheet (1 cm^2, 99.99%) was obtained from Sigma-Aldrich. All the purchased chemical reagents were analytical grade and were utilized as received without further purification.

2.2. Synthesis of N-doped 2D graphene derivatives

Synthesis of the N-2D GDs proceeded *via* a controlled hydrothermal treatment of glucose, utilizing small concentrations of CTAB and ammonia as structure-directing agents. Typically, 0.5 M of aqueous glucose solution was prepared and then CTAB powder was dissolved into it in various small CTAB/glucose molar ratios. Lastly, traces of ammonium hydroxide solution was added to the mixture with a volumetric ratio of 1/10 to make the pH of the solution pH $\sim$11. The whole mixture was then sealed in a Teflon-lined stainless-steel autoclave system at a vapor/liquid volumetric ratio of 3/2 and thermally treated in an oven (Nabertherm, TR60, UK) for 4 h at different temperatures of 250 °C and 270 °C. Various CTAB/glucose molar ratios of 0, 1/9, and 1/6 were investigated, by precisely dissolving 0, 1.7, and 3.4 g of CTAB, respectively, in 100 ml of 0.5 M aqueous glucose solution, at the hydrothermal process temperature of 250 °C. While at the hydrothermal process temperature of 270 °C, a fixed CTAB/glucose molar ratio of 1/6 was employed. After the hydrothermal treatment, the autoclave system was slowly cooled to ambient temperature and then opened to obtain the formed product. A dark brownish black slurry was formed in the Teflon tube when the hydrothermal treatment was conducted at 250 °C; whereas at 270 °C, the product distinctively resembled fluffy expanded black solid platelets. Finally, the obtained carbon products were filtered, washed several times with distilled water, and then dried in a vacuum oven at 70 °C for two days. The codes for the produced carbon samples are listed in Table 1.

NG refers to the N-doped 2D graphene derivative. NCD, LCD, and HCD refer to the employed no (0), low (1/9), and high (1/6) doses of CTAB during synthesis, respectively. Lastly, the number refers to the employed hydrothermal synthesis temperature.

2.3. Structural characterizations

Fourier transform infrared (FTIR) spectroscopy was utilized to qualitatively investigate the oxidation state of the carbonaceous samples, using a Shimadzu FTIR-8400S spectrometer (Shimadzu Corporation, Kyoto, Japan). The FTIR spectrum of CTAB was also recorded, using the same equipment and analysis conditions, to gather information about the functionalization of the carbonaceous samples with CTAB. X-Ray photoelectron spectroscopy (XPS) were employed to determine the C, O, and N concentrations within the carbonaceous samples, which enabled the quantitative estimation of the oxidation state and N-doping level. Further, XPS could indicate the various configurations of the doped N atoms within the graphitic lattice. The XPS analysis was implemented using a Kratos Axis Ultra DLD X-ray photoelectron spectrometer (Kratos Analytical Ltd, Manchester, UK). Raman spectroscopy measurements for characterization of the crystal structural order within the sp^2 C-network of the carbonaceous samples were performed using a Bruker SENTERRA Raman microscope (Bruker Corporation, Ettlingen, Germany), with 532 nm laser excitation. This could provide information on the in-plane crystal size, types, extent of crystal defects, and degree of stacking of the carbon layers. Finally, the surface morphology of the carbonaceous samples was monitored by scanning electron microscopy (SEM, JEOL, Model JSM 6360 LA, Japan) and high-resolution transmission electron microscopy (HR-TEM, JEOL JEM-2100).

Table 1 Codes of carbon samples

Sample code	Hydrothermal synthesis conditions	
	CTAB dose (CTAB/glucose molar ratio)	Hydrothermal temperature (°C)
NG-NCD250	0	250
NG-LCD250	1/9	
NG-HCD250	1/6	
NG-HCD270	1/6	270

The sample preparations for the various analyses and testing conditions were typical to those reported in our previous study.[17]

2.4. Electrode preparation and electrochemical measurements

The working electrode was prepared as follows. The as-prepared N-2D GD powder (90 wt%), carbon black (5 wt%) as an additive material, polyvinylidinefloride (PVDF) (5 wt%) as a binder, and 1-methyl 2-pyrrolidinone as a solvent were mixed, forming a slurry. The slurry was then coated onto nickel (Ni) sheet (1 cm^2) and dried at 60 °C overnight. The mass of active material (N-2D GD powder) in the active surface was around 1 mg cm^{-2}. The Ni sheet was pre-cleaned before being coated, by dipping in HCL solution for 30 min to remove the nickel oxide (NiO) layer from the surface and then washing with deionized water and ethanol to remove any impurities from the surface. Finally, it was dried in a vacuum oven at 50 °C for 30 min.

The electrochemical measurements of the N-2D GDs-based electrodes were performed in a symmetric two-configuration electrode cell with equal electrode masses, using nickel sheet as a current collector and Whatman fiber glass filter paper (GF/D) as a separator. The used electrolyte was 2 M Na_2SO_4. The measurements were performed at room temperature using a computer-controlled potentiostat (Metrohm Autolab, Model: 87070), involving cyclic voltammetry (CV), galvanostatic charge/discharge (GCD), and electrochemical impedance spectroscopy (EIS). The CV studies were performed between 0 to 1 V at a sweep rate of 100 mV s^{-1}. The charge–discharge measurements were performed at a current density of 1 A g^{-1}. The specific capacitance (C), energy density

(E), and power density (P) of the electrode were calculated from the corresponding GCD curve, using eqn (1)–(3) respectively:

$$C = \frac{I \times \Delta t}{m \times \Delta V} \quad (1)$$

$$E = \frac{C \times \Delta V^2}{2 \times 3.6} \quad (2)$$

$$P = \frac{E \times 3600}{\Delta t} \quad (3)$$

where I, Δt, ΔV, and m are the discharge current (A), discharge time (s), potential window (V), and the mass of the active material on a single electrode (g), respectively.

The EIS measurements were carried out in the frequency range of 1 mHz to 100 kHz at an open-circuit potential with a small AC perturbation of amplitude of 5.0 mV. The phase angle and the equivalent series resistance (ESR) were estimated from the produced Nyquist plots.[6,18]

Further electrochemical measurements were conducted on the graphitic sample-based electrode that exhibited the best electrochemical capacitive performance, including rate capability, cyclic stability, and EIS spectrum fitting with the equivalent circuit model.

3. Results and discussion

3.1. Structural characteristics

The graphitic nature of all the prepared carbonaceous samples was evidenced by the FTIR, XPS, and Raman analyses, as explained in the following discussion. On the other hand, the oxidation state of the graphitic structure was qualitatively investigated by FTIR and quantitatively estimated by XPS analysis.

The FTIR spectra of the carbonaceous samples prepared at a hydrothermal temperature of 250 °C and varied CTAB doses (0, 1/9, 1/6 CTAB/Glucose molar ratio) and those of carbonaceous samples prepared at the highest CTAB dose (1/6 CTAB/Glucose molar ratio) and varied hydrothermal temperatures (250 °C, 270 °C) are presented in Fig. 1a and b, respectively. The appearance of the IR absorption peak (1600–1670 cm^{-1}) in all the spectra, corresponding to the in-plane cyclic C=C vibration,[19,20] evidenced the graphitic nature of all the carbonaceous samples.

The presence of oxygen functional groups in the graphitic structure was evident for all the prepared samples at 250 °C (Fig. 1a), as their FTIR spectra showed obvious peaks at ~3430, ~1160, and ~1040 cm^{-1}, which could be ascribed to O–H stretching, epoxy C–O–C, and alkoxy C–O vibrations, respectively. In addition, a band attributed to O–H bending was apparent at ~1430 cm^{-1} for the graphitic sample produced at a zero dose of CTAB (NG-NCD250).[19,21] It could be clearly noticed that as the CTAB dose increased, the O–H stretching band at 3430 cm^{-1} was significantly reduced. The epoxy and alkoxy bands showed fair reductions in their intensities. Additionally, the C=C band was shifted downward from 1622.2 to 1620.2 and 1608 cm^{-1}, respectively. Thus, a reasonable deoxygenation of the graphitic structure could be achieved by increasing the CTAB dose, with a major degree in the NG-HCD250 sample. Fig. 1b shows that the increase in hydrothermal temperature to 270 °C at the highest CTAB dose diminished the oxygenation level of the graphitic structure by a considerable extent. Thus, the band ascribed to O–H stretching at 3430 cm^{-1} was clearly much weaker in NG-HCD270, compared to in NG-HCD250. Moreover, the epoxy and alkoxy bands almost disappeared in NG-HCD270, indicating the extremely tiny oxidation state of the NG-HCD270 sample.

On the other hand, FTIR analysis of the graphitic samples prepared in the presence of CTAB revealed their functionalization by CTAB molecules. The FTIR spectrum of CTAB, displayed in Fig. 2, exhibited major bands at 3430, 2920/2850, 1470/1395, 910/968, and 727 cm^{-1}, designated to N–H stretching, symmetric and asymmetric CH_2 stretching of the backbone chain, asymmetric and symmetric C–H scissoring of the N–CH_3 moiety, C–N stretching, and CH_2 rocking vibration of the backbone chain, respectively.[22,23]

In the FTIR spectra of the graphitic samples prepared at hydrothermal temperature of 250 °C and different CTAB doses

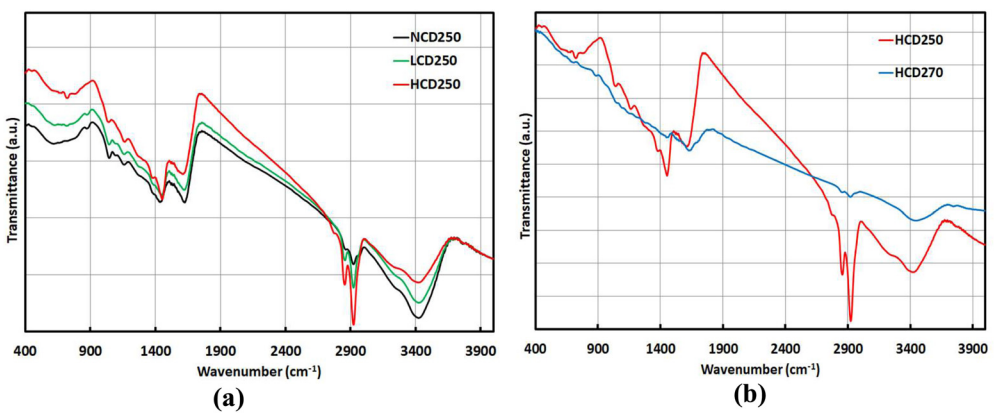

Fig. 1 FTIR spectra of the synthesized graphitic samples at (a) varying CTAB doses and a fixed hydrothermal temperature of 250 °C, (b) varying hydrothermal temperatures and the fixed highest CTAB dose.

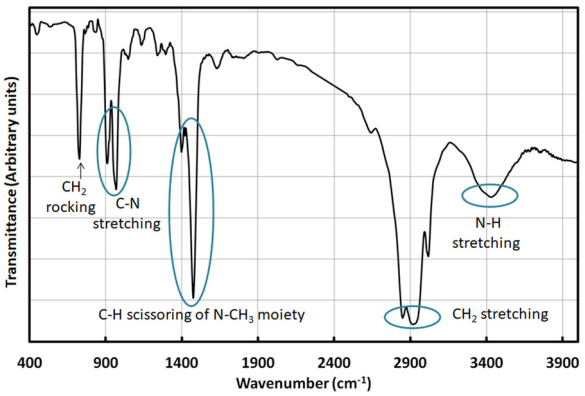

Fig. 2 FTIR spectrum of CTAB.

(Fig. 1a), it could be clearly noticed that the bands around 2920 and 2850 cm^{-1} were enhanced with increasing the dose of CTAB. Furthermore, the band at 1430 cm^{-1}, assigned to OH bending vibration in the NG-NCD sample, was shifted upward to ~1450 cm^{-1} and was intensified with the increase in CTAB dose, which implied an overlap with the N-CH_3 band of CTAB at 1470 cm^{-1}. In addition, a shoulder appeared at ~1380 cm^{-1}, which could be correlated to the N–CH_3 band of CTAB at 1395 cm^{-1}. These three observations evidenced that the NG-LCD and NG-HCD samples were functionalized by CTAB and the density of capping CTAB molecules on the graphitic structure surface was significantly higher in the NG-HCD sample than in the NG-LCD sample. Conversely, Fig. 1b shows that the characteristic FTIR bands correlated to CTAB were much diminished with increasing the hydrothermal temperature from 250 °C to 270 °C at the highest CTAB dose, indicating the lowest density of capping CTAB molecules on the graphitic structure surface in the NG-HCD270 sample.

The XPS analysis agreed well with the FTIR analysis and quantitatively confirmed the modest deoxygenation of the graphitic samples with the increased CTAB dose at the hydrothermal temperature of 250 °C, which became much more significant with increasing the hydrothermal temperature to 270 °C at the highest CTAB dose. The high-resolution XPS spectra revealed the constitution of the graphitic samples with C, O, and N elements. The elemental composition data as atomic percentages (at%) for the graphitic samples are listed in Table S1 in the ESI.† The C/O atomic ratio for the graphitic samples increased from ~11.9 to ~14 to ~15 as the CTAB dose increased from 0 to 1/9 to 1/6, respectively, at the hydrothermal temperature of 250 °C. Further, the C/O atomic ratio increased to ~16 when the hydrothermal temperature was raised to 270 °C at the highest CTAB dose. On the other hand, the deconvolution of the C1s spectra for the graphitic samples showed that carbon atoms were present in different functional groups, as can be seen in Fig. 3. For the NG-NCD250 sample, bands for the non-oxygenated ring C (the sp^2carbon (C═C)) at ~284.7 eV, the C–OH and C–N at ~286.5 eV, the C–O–C, C═O, and C═N at ~287.8 eV, and the O–C═O at ~288.9 eV were apparent.[24,25] For the graphitic samples prepared in the presence of CTAB, the carboxylic band at ~288.9 eV completely

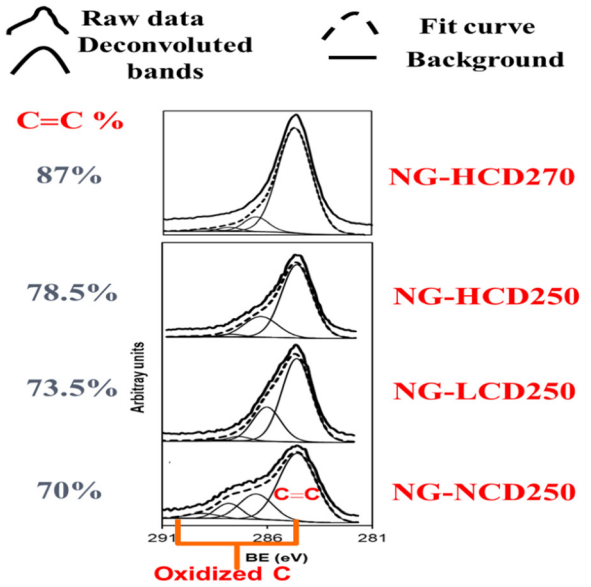

Fig. 3 XPS C1s spectra of graphitic samples.

disappeared and the other oxygenated carbon bands became weaker with increasing the CTAB dose and were also much more diminished at the higher hydrothermal temperature. Thus, the percentage of the graphitic sp^2 carbon peak was boosted from 70% to 78.5% as the CTAB dose increased from 0 to the highest value. Then, it further increased to 87% upon increasing the hydrothermal temperature to 270 °C at the highest CTAB dose.

In our recent previous study,[8] it was disclosed that the origin of the synergistic deoxygenation phenomenon of the graphitic structure with the increased CTAB dose and, further, with the higher hydrothermal temperature was related to the chemical decomposition behavior of CTAB under hydrothermal synthesis conditions. In such study, TGA analysis revealed the propagated chemical decomposition of CTAB at higher temperature in the temperature range of 210–310 °C. It was noticed that the thermal decomposition of CTAB was fair at 250 °C and significant at 270 °C by the weight losses of 15% and 49%, respectively (Fig. 4). Thus, the concentrations of evolved hydrogen-containing gases through the hydrothermal synthesis system, which are responsible for deoxygenation of the graphitic structure, followed the same trend. This explains why the role of the increased CTAB dose in deoxygenating the graphitic structure was only fair at 250 °C. It also clarifies why the CTAB influence in deoxygenating the graphitic structure was most efficient at 270 °C, as revealed by the FTIR and XPS analyses. The modest effect of the CTAB dose compared to the significant effect of hydrothermal temperature was expected, because increasing the CTAB dose from 1/9 to 1/6 intensified the evolved hydrogen-containing gases by 50%, whereas the increased hydrothermal temperature intensified the evolved hydrogen-containing gases by 227%.

It is worth mentioning that the little functionalization degree of the graphitic structure surface by CTAB in the NG-HCD270 sample could also be attributed to the significant

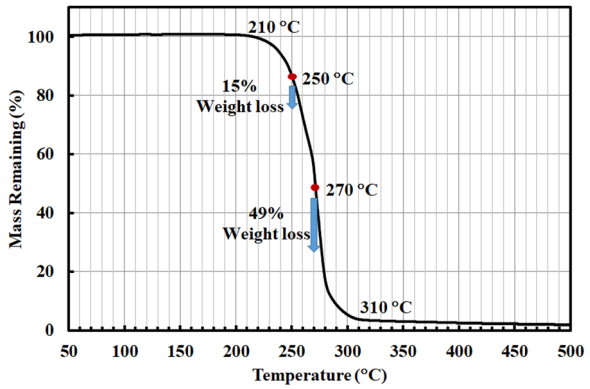

Fig. 4 TGA analysis of CTAB.

chemical decomposition of CTAB at 270 °C, which reduced the concentration of undecomposed CTAB molecules in the reaction medium.

Regarding the doping of graphitic samples with nitrogen, the presence of the N element within the graphitic structure was proved by the XPS analysis. The N/C atomic ratio results presented in Fig. 5a interestingly reveal that the total N content within the graphitic material decreased with increasing the CTAB dose while it was insensitive to temperature variation during the hydrothermal synthesis. Additionally, XPS analysis gives information about different bonding configurations of doped N atoms in the carbon lattice. The high-resolution N1s spectra of the graphitic samples are presented in Fig. 5b. The deconvolution peaks of the N1s spectra showed that in the NG-NCD250 sample there existed two different N components corresponding to pyridinic N (~398.7 eV) and pyrrolic N (~399.9 eV).[26,27] Interestingly, when CTAB was present during the hydrothermal synthesis process, besides the pyridinic N and pyrrolic N peaks, an additional peak appeared at ~402.5 eV, assigned to pyridinic-oxide N (NO_x) species.[4,27–29] The one exception was the NG-HCD270 sample, in which the peak corresponding to pyridinic NO_x species disappeared and graphitic N (~401.8 eV)[26,27] became present with pyridinic N and pyrrolic N components.

The detection of doped pyridinic NO_x species within the carbon lattice of the graphitic samples, synthesized in the presence of CTAB, did not evidence a higher oxidation state of such samples. This is because it has already been proved that the NG-LCD250 and NG-HCD250 samples possessed significantly lower oxidation states than the NG-NCD250 sample *via* two analyses techniques: FTIR and XPS. It can be speculated that the interactions between the CTAB molecules and graphitic structure, dominated by functionalization of the graphitic structure surface by CTAB, were mainly responsible for the main realized N-doping phenomena: the decreased total doped N content within the graphitic material with the increase in CTAB dose and the doped pyridinic NO_x species within the carbon lattice of the synthesized graphitic samples in the presence of CTAB. The CTAB molecules, capping the graphitic structure surface, can be considered as a covering cloud around the graphitic material. Thus, the increase in density of the capping CTAB molecules on the graphitic structure surface with the increase in CTAB dose most probably hinders the penetration of N atoms into the graphitic structure, therefore resulting in a lesser degree of graphitic structure doping with N atoms. On the other hand, the origin of the doped pyridinic NO_x species within the carbon lattice of the synthesized graphitic samples in the presence of CTAB (NG-LCD250, NG-HCD250) was most probably due to electrostatic interaction between the ammonium head of CTAB and the oxygen functional groups on the graphitic structure surface. The subsequent thermal decomposition of CTAB and oxygen functional groups under the hydrothermal synthesis conditions leaves NO_x species in

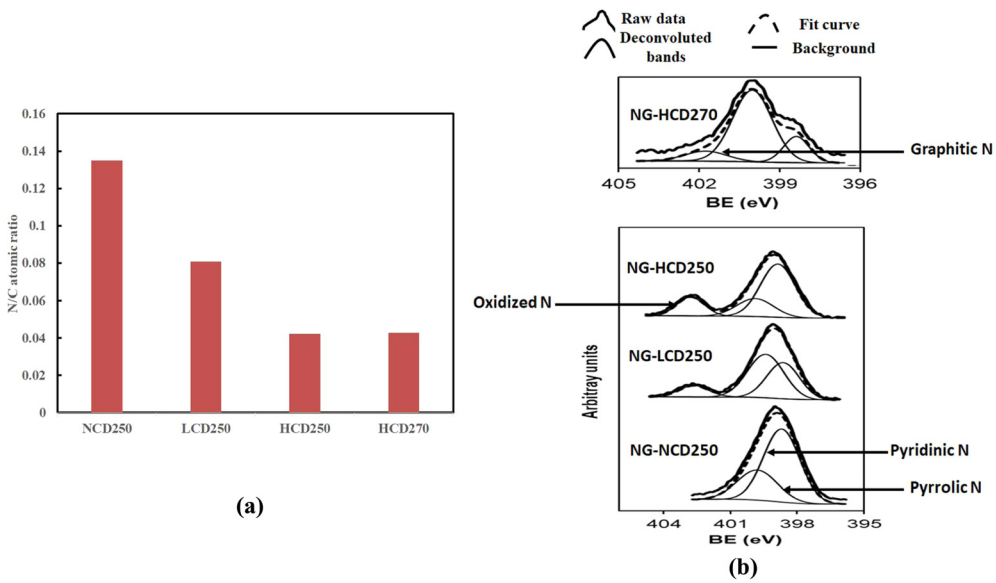

Fig. 5 (a) N/C atomic ratio from XPS analysis and (b) XPS N1s spectra of graphitic samples.

the carbon lattice of the graphitic structure. The excessive removal of oxygen functional groups from carbon lattice during the formation of the NG-HCD270 sample often causes the conversion of the doped pyridinic NO_x to graphitic N.

Raman analysis was next employed to investigate the structural order and defects within the sp^2-carbon lattice of the graphitic samples. The Raman spectra of the graphitic samples prepared at a hydrothermal temperature of 250 °C and varied CTAB doses and those of graphitic samples prepared at the highest CTAB dose and varied hydrothermal temperatures (250 °C, 270 °C) are presented in Fig. S1a and b in the ESI,† respectively. All the spectra showed the characteristic Raman D (~1355–1380 cm^{-1}) and G (1565–1580 cm^{-1}) bands of graphitic materials, which arose from the graphitic lattice disorder and the in-plane vibration of aromatic sp^2 carbon (C═C), respectively. It is worth mentioning that the graphitic lattice disorder originated from defects associated with vacancies, grain boundaries, amorphous carbon species, sp^3 carbon species, and the incorporation of foreign atoms or molecules within the aromatic sp^2 C-network.[21,30]

The Raman spectra of the graphitic samples were deconvoluted using Origin pro9 software to determine the nature of the constituent carbon species and to obtain detailed information on the structural order within the graphitic structure. The deconvoluted Raman spectra of the NG-NCD250, NG-LCD250, NG-HCD250, and NG-HCD270 graphitic samples in the range of 1000–1800 cm^{-1} are presented in Fig. 6a–d, respectively. A total of five peaks were fitted and were designated as G, D1, D2, D3, and D4, following the Lorentzian distribution, which indicated the presence of different C atoms structures within the graphitic samples. The G band at about 1540–1560 cm^{-1} and also the D2 band at about 1598–1611 cm^{-1} are known to arise from the graphitic-like planes, due to the in-plane vibration of graphitic sp^2 carbon (C═C). The D1 band located at about 1337–1362 cm^{-1} was due to the graphitic lattice disturbance at sp^2-C crystallites boundaries, which emerges as zone boundary disorder. The D3 band at about 1485–1520 cm^{-1} originated from the amorphous carbon fraction (sp^3 carbon and aliphatic sp^2 carbon chain). The D4 band at about 1117–1165 cm^{-1} was likely due to the mixed vibrations of sp^3–sp^2 bonds (C–C and C═C stretching) or the increased defects in the graphitic lattice by oxidation.[31–33] The D3 band, which belongs to the amorphous carbon fraction, disappeared in the synthesized graphitic samples in the presence of CTAB (NG-LCD250, NG-HCD250, and NG-HCD250). This indicates a higher degree of graphitization (aromatic sp^2–carbon content) with improved structural order within such graphitic samples compared to the NG-NCD sample. On the other hand, a well-distinguished additional peak at 1420 cm^{-1} was observed in the NG-LCD250 sample. This was upward shifted to higher wavenumber at 1440 cm^{-1} in the NG-HCD250 sample by increasing the CTAB dose during synthesis. With increasing the hydrothermal synthesis temperature to 270 °C, such additional band exhibited a downward shift to

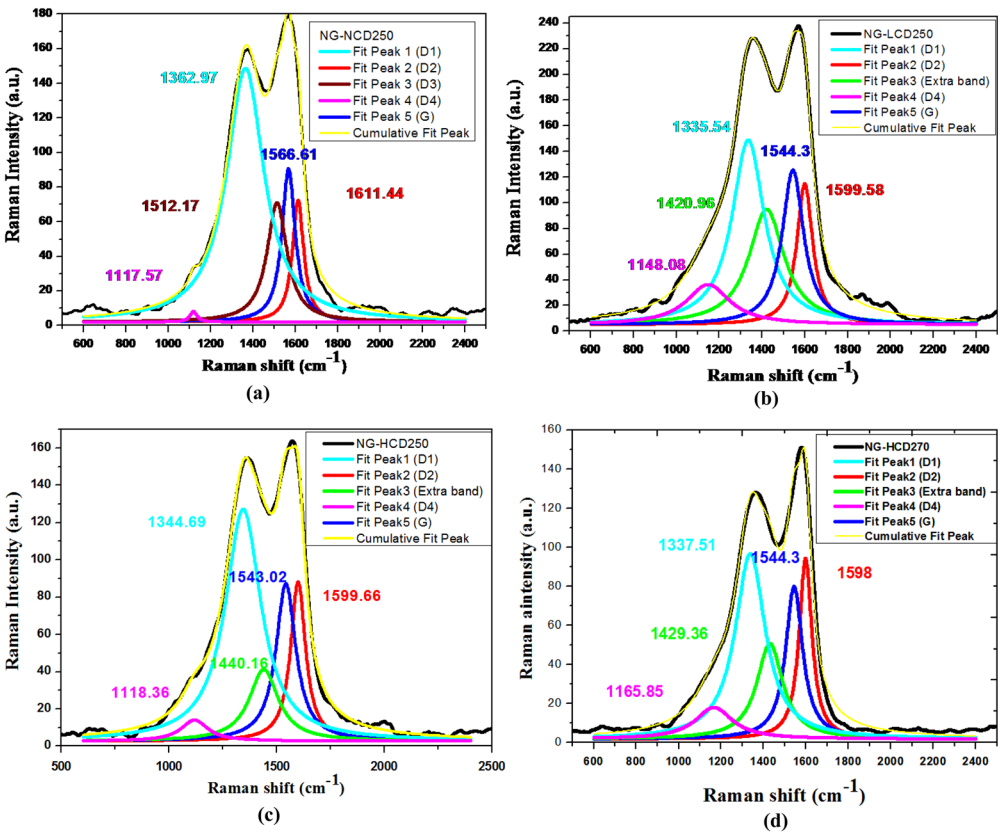

Fig. 6 Deconvoluted Raman spectra of the (a) NG-NCD250, (b) NG-LCD250, (c) NG-HCD250 and (d) NG-HCD270 graphitic samples.

1429 cm^{-1} in the NG-HCD270 sample. Such an additional peak can be attributed to the asymmetric C–H bending vibration (scissoring mode) of an N–CH_3 moiety and/or bending vibration of a CH_2 group within the CTAB molecule in the range of 1430–1470 cm^{-1}.[33] This observation agreed well with the FTIR analysis, confirming the surface functionalization of the NG-LCD250, NG-HCD250, and NG-HCD250 samples by CTAB molecules.

The ratios of intensities of the D1 to G peaks (I_{D1}/I_G) and D1 to D2 peaks (I_{D1}/I_{D2}) were calculated for quantitative estimation of the type and concentration of defects within the graphitic samples. In addition, the average in-plane crystallite size (lateral size) of the aromatic sp^2 domains (La) was calculated using the Tuinstra and Koenig relation,[34] which is indicated below:

$$La = C(\lambda)\ (I_{D1}/I_G)^{-1} \quad (4)$$

where the coefficient $C(\lambda)$ is a wavelength dependent prefactor ($\sim$4.4 nm). The data are presented in Table 2.

The data in Table 2 indicate that the three synthesized graphitic samples in the presence of CTAB (NG-LCD250, NG-HCD250 and NG-HCD270) have lower I_{D1}/I_G ratios than the NG-NCD250 graphitic sample. This reveals the reduced zone boundary disorder within the graphitic lattices of such graphitic samples compared to in the NG-NCD sample, most probably due to lower oxidation and N-doping levels. Meanwhile, the three synthesized graphitic samples in the presence of CTAB displayed higher average in-plane crystallite sizes than the NG-NCD sample, indicating the improved interior structural order and perfection of the aromatic sp^2-c crystals within those three graphitic samples compared to the NG-NCD sample. It could be noticed that the NG-HCD250 sample had the worst structural order at the grain boundary zones and interior aromatic sp^2-c crystals among the three synthesized graphitic samples in the presence of CTAB, probably because of its densest graphitic surface functionalization by CTAB molecules.

On the other hand, the I_{D1}/I_{D2} intensity ratio is also closely related to the amount and type of defects present within the graphitic structure. There are three types of defects in graphene systems, which can be estimated based on the I_{D1}/I_{D2} intensity ratios, namely (i) hopping defects, originating from the distortion of carbon bonds, (ii) on-site defects, arising due to the out-of-plane atoms bonded to carbon atoms, which is useful for describing the sp^3 hybridized phase, and (iii) charged impurity, resulting from the presence of charged impurities. The reported value of $I_{D1}/I_{D2} \sim 10.5$ indicates hopping defects, while when it is about 1.3 it indicates on-site defects.[35,36] The I_{D1}/I_{D2} ratios were found to be 2.088, 1.31, 1.45, and 1.02 for the NG-NCD, NG-LCD250, NG-HCD250, and NG-HCD270 graphitic samples, respectively. This indicates that the defects could be attributed to the combination of on-site and hopping defects in the NG-NCD sample, while they were mainly due to on-site defects in the three synthesized graphitic samples in the presence of CTAB. In addition, based on the I_{D1}/I_{D2} value, it could be estimated that the amount of defects was highest in NG-NCD250, medium in NG-HCD250, low in NG-LCD250, and lowest in the NG-HCD270 sample.

The morphologies of the graphitic samples were explored *via* SEM and HR-TEM analyses. The SEM micrographs of the graphitic samples are given in Fig. 7 and 8. Low- and high-magnification SEM images of the NG-NCD250 and NG-LCD250 graphitic samples are in series presented in Fig. 7 parts (a and b) and (c and d), respectively. The NG-NCD250 sample showed a mixed spherical/sheet architecture, as shown in Fig. 7(a and b). The sheet architecture consisted of bulky micro-sized sheets with big thickness of up to 15 μm (Fig. 7(a)). In the magnified images (Fig. 7(b)), the thick micro-sized sheets appear fairly exfoliated into considerably thinner sub-micron sheets.

With the addition of a low dose of CTAB during the hydrothermal synthesis process, the NG-LCD250 sample possessed a minor concentration of spherical particles and the bulky micro-sized sheets exhibited a significant degree of exfoliation into very thin sheets, with small thicknesses down to the nano-sized range (Fig. 7(c and d)). Interestingly, with a high dose of CTAB used during the hydrothermal synthesis, the observed morphologies of the NG-HCD250 and NG-HCD270 graphitic samples became substantially different, as displayed by their SEM images in Fig. 8 and Fig. S2, S3 in the ESI.† The NG-HCD250 sample (Fig. 8(a and b) and Fig. S2 in the ESI†) showed only a sheet morphology, which manifested extensive exfoliation, and the spherical particles had completely disappeared. The low-magnification images indicated that small micro-sized sheets with short lateral dimensions in the range of 1.5–35 μm dominated the architecture. The high-magnification images further clearly reveal that the micro-sized sheets had been extensively exfoliated into very thin nanosheets. The morphology of the NG-HCD270 sample was even more amazing. Two different regions could be see within the sample, as displayed in Fig. 8(c and d) and Fig. S3 in the ESI.† Well-separated very thin sheets, having a large flat surface with long lateral dimensions up to 350 μm, prevailed throughout the architecture. The surfaces of the sheets comprised some folding and wrinkled areas, indicating a high flexibility of the sheets owing to their extremely fine thickness.

The morphologies of the graphitic samples were further deeply explored by HR-TEM microscopy (Fig. 9 and 10). The

Table 2 Deconvoluted Raman analysis data of graphitic samples

Sample code	I_{D1}/I_G	La (nm)	I_{D1}/I_{D2} Value	Type of defects	Amount of defects
NG-NCD250	1.656395	2.6563709	2.088	Combination of on-site and hopping defects	Highest
NG-LCD250	1.192691	3.6891376	1.3109	On-site defects	Low
NG-HCD250	1.475042	2.9829655	1.455	On-site defects	Medium
NG-HCD270	1.217176	3.6149262	1.025	On-site defects	Lowest

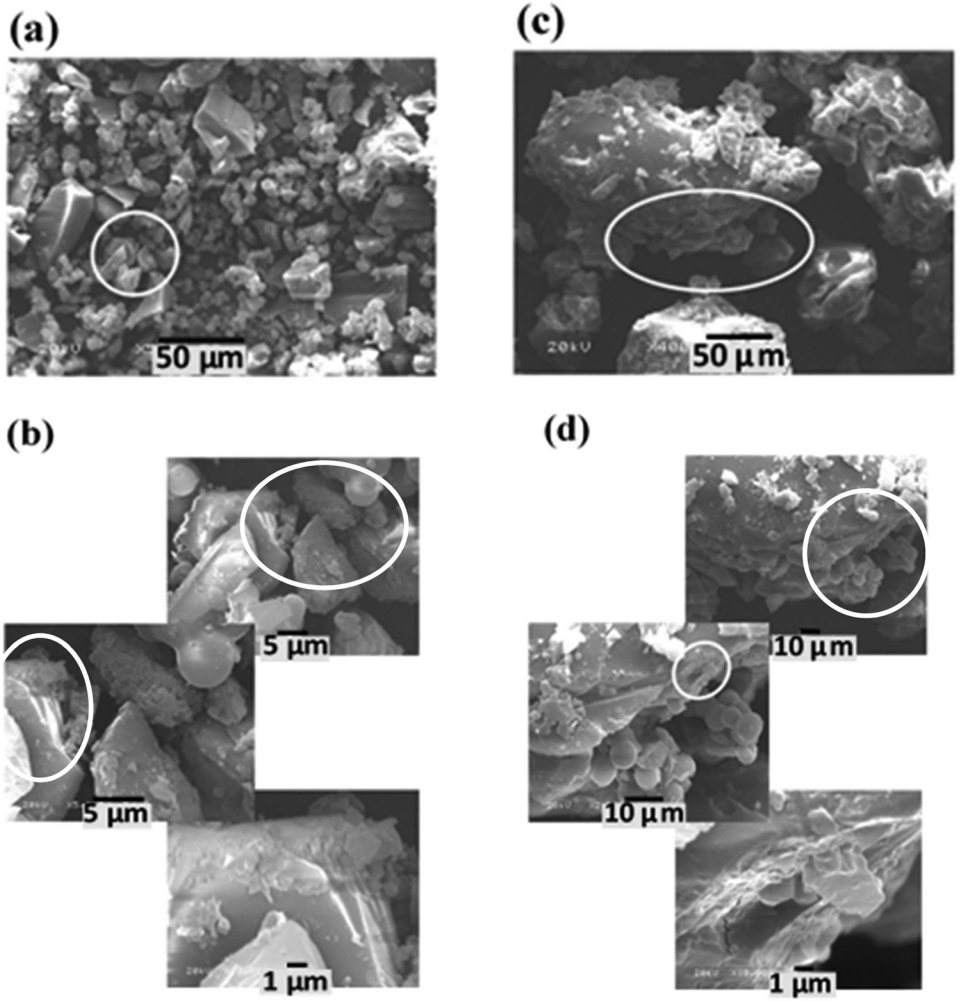

Fig. 7 SEM micrographs captured from low to high magnification for the (a) and (b) NG-NCD250 and (c) and (d) NG-LCD250 graphitic samples.

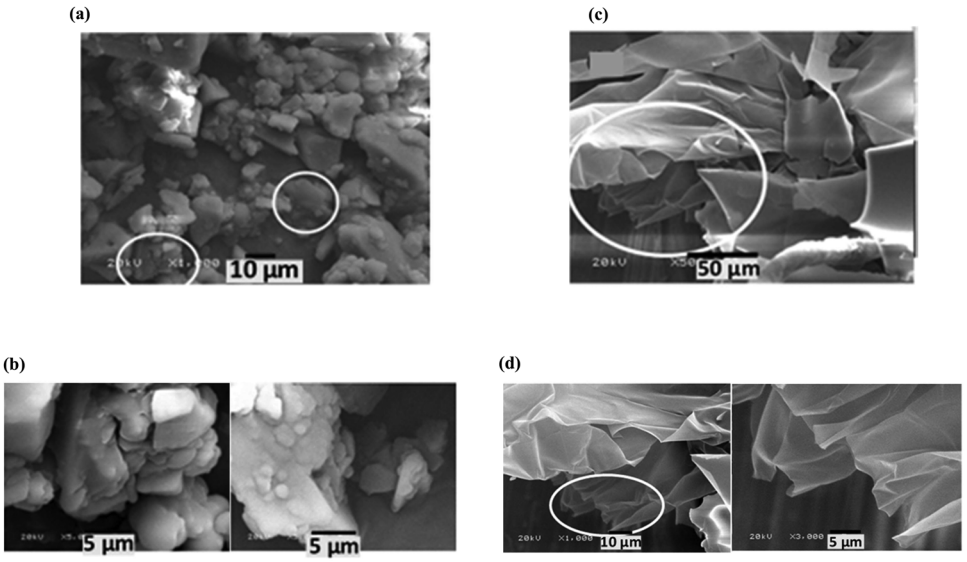

Fig. 8 SEM micrographs captured from low to high magnification for the (a) and (b) NG-HCD250 and (c) and (d) NG-HCD270 graphitic samples.

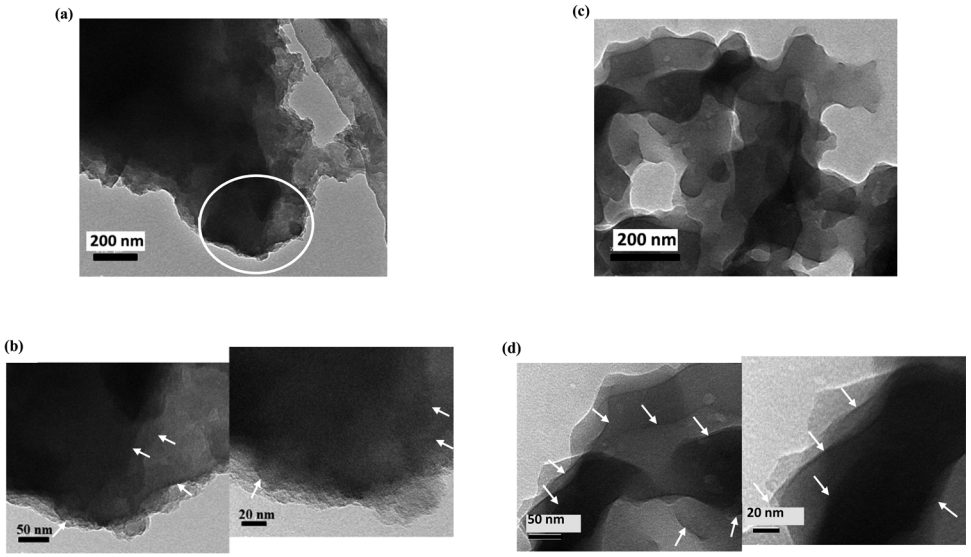

Fig. 9 HR-TEM micrographs captured from low to high magnification for the (a) and (b) NG-NCD250 and (c) and (d) NG-LCD250 graphitic samples.

low- and high-magnification HR-TEM images of the NG-NCD250 and NG-LCD250 graphitic samples are in series presented in Fig. 9 parts (a and b) and (c and d), respectively, and those of NG-HCD250 and NG-HCD270 graphitic samples are in series presented in Fig. 10 parts (a and b) and (c and d), respectively.

The low-magnification images showed that dark bulky nanoflakes dominated the architecture in the NG-NCD250 (Fig. 9(a)) and NG-LCD250 (Fig. 9(c)) graphitic samples; whereas the NG-HCD250 (Fig. 10(a)) and NG-HCD270 (Fig. 10(c)) graphitic samples consisted of fluffy multilayered nanosheets.

The high-magnification images of the NG-NCD250 sample showed that the massive dark bulky nanoflakes were composed of a number of thinner nanosheets but they appeared to be lumped together (Fig. 9(b)); so single graphene layers were not distinguishable and could not be accurately counted even at very high magnification, *i.e.*, down to the scale bar of 10 nm. In the NG-LCD250 sample, the constituent thin nanosheets of the bulky nanoflakes appeared to be fairly exfoliated in the high-magnification HR-TEM images (Fig. 9(d)); however, they still looked dark with coarse edges, implying that such distinguished separate graphitic layers did not represent a single

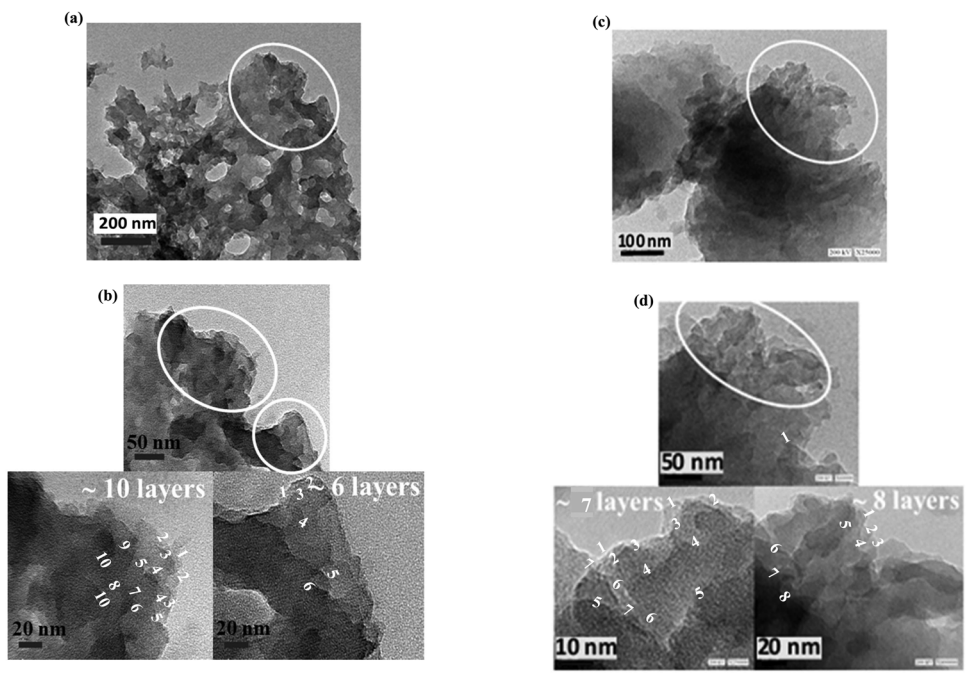

Fig. 10 HR-TEM micrographs captured from low to high magnification for the (a) and (b) NG-HCD250 and (c) and (d) NG-HCD270 graphitic samples.

graphene nanosheet but were either bi-layered or tri-layered graphene nanosheets, *i.e.*, each detectable layer could be considered a few-layered graphene nanosheet. So, again, single graphene layers could not be accurately counted even at very high magnification. The apparent dark and coarse graphitic layers in the high-magnification HR-TEM images of the NG-NCD250 and NG-LCD250 graphitic samples, which evidenced a number of overlapping single graphene layers, are denoted by white arrows in the figures for simple clarification.

Impressively, the high-magnification HR-TEM images revealed good exfoliation of the fluffy multilayered nanosheet architecture for both the NG-HCD250 (Fig. 10(b)) and NG-HCD270 (Fig. 10(d) and Fig. S4 in the ESI†) samples. It could be noticed that NG-HCD250 (Fig. 10(b)) consisted of a multilayered interrupted network of small nanosheets while NG-HCD270 (Fig. 10(d)) consisted of large multilayered nanosheets with a continuous structure, which supports the SEM observations, confirming the significantly smaller lateral size, and therefore, the surface area of the nanosheets within NG-HCD250 than in NG-HCD270. Further, the extreme high magnifications of the multilayered nanosheets architectures within the NG-HCD250 and NG-HCD270 samples revealed that they were composed of clearly distinguishable separated graphitic layers. Here, each distinguishable layer is denoted by a number, appearing through the layer length, indicating how the layers flow. Thus, ~6–11 separated graphitic layers could be distinguished upon magnifying the small multilayered nanosheet architecture within various regions of the NG-HCD250 sample (Fig. 10(b)). The large nanosheets architectures in the NG-HCD270 sample appeared more exfoliated, composed of ~5–9 separated graphene layers, as can be seen in Fig. 10(d) and Fig. S4 in the ESI.†

3.2. Electrochemical performance

The electrochemical energy-storage performances of symmetric two-electrode supercapacitor systems based on NG-NCD250, NG-LCD250, NG-HCD250, and NG-HCD270 electrodes, are presented and discussed below.

The cyclic voltammetry (CV) curves of two-electrode cells based on NG-NCD250, NG-LCD250, NG-HCD250, and NG-HCD270 electrodes at a scan rate of 100 mV s^{-1} are presented in Fig. 11. The CV curve of the NG-HCD270 sample exhibited a typical quasi-rectangular shape, indicating that the charge-storage capacitance of such a sample mainly comes from the EDLC storage mechanism. On the other hand, the CV curve of the NG-NCD250 sample seemed to deviate a little bit from quasi-rectangular shape. Furthermore, there were obvious significant deviations from the rectangular shape for the CV curves of the NG-LCD250 and NG-HCD250 samples. The distortion in the rectangular shape of the CV curve evidences an induced pseudocapacitive contribution besides the EDLC mechanism in the charge-storage behavior. The doped pyridinic-oxide N (NO_x) followed by pyrrolic N within the graphitic structure are mainly responsible for charge storage by the pseudocapacitive behavior.[4,12,37,38] Thus, most probably, the considerable charge storage contributed by the pseudocapacitive behavior for the NG-LCD250 and NG-HCD250 samples originated mainly from the pyridinic doped-NO_x and pyrrolic N species within their graphitic structure. The doped-pyrrolic N in the graphitic structure of the NG-NCD250 sample prompted a small charge-storage portion due to the pseudocapacitive behavior in such samples. However, although pyrrolic N was the dominant doped-N configuration in the NG-HCD270 sample, the much lower total doped-N content (N/C atomic ratio = 0.042) compared to the case in the NG-NCD250 sample (N/C atomic ratio = 0.135), which reached down to about one-third, led to trivial charge storage from the pseudocapacitive behavior. Therefore, the charge storage by the EDLC storage mechanism prevailed in such a sample.

On the other hand, it could be noticed that the enclosed area of the CV curve was largest for the NG-HCD270 sample, followed by the NG-LCD250 sample, then the NG-NCD250 sample, and lastly the NG-HCD250 sample. This implies that the NG-HCD270 sample possessed the maximum energy-storage capacitance, followed by the NG-LCD250 sample, then the NG-NCD250 sample, and lastly the NG-HCD250 sample.

The galvanostatic charge–discharge (GCD) curves of two-electrode cells based on the NG-NCD250, NG-LCD250, NG-HCD250, and NG-HCD270 electrodes at a current density of 1 A g^{-1} are presented in Fig. 12. The charge-storage specific capacitance data for the four graphitic samples-based electrodes were calculated from the corresponding GCD curves, using eqn (1). Also, their storage energy and power densities were estimated using eqn (2) and (3). The data are listed in Table 3.

The data in Table 3 reveal that the NG-HCD270 electrode possessed the maximum specific capacitance and consequently energy-storage density, followed by the NG-LCD250 electrode, then the NG-NCD250 electrode, and lastly the NG-HCD250 electrode. These results agreed well with the inferences from the CV curves. The interpretations of the electrochemical performances for the four graphitic samples from the perspective of their nanostructure characteristics will be clear after analyzing the impedance behavior of the four graphitic samples.

The Nyquist plots, obtained from electrochemical impedance spectroscopy (EIS) measurements allowed elucidating the frequency-dependent behavior of the prepared electrodes. The Nyquist plots for the NG-NCD250, NG-LCD250, NG-HCD250 and NG-HCD270 electrodes are presented in Fig. 13(a).

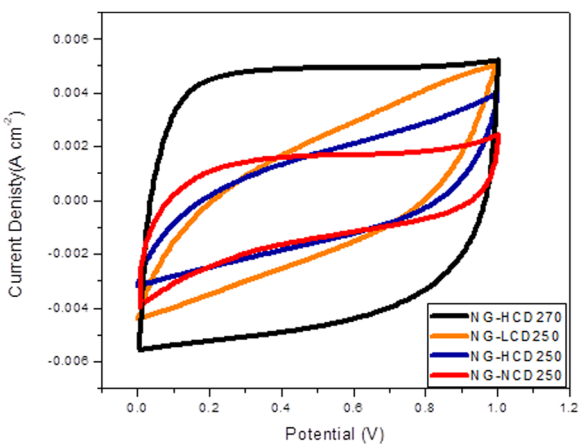

Fig. 11 Cyclic voltammetry curves of graphitic samples.

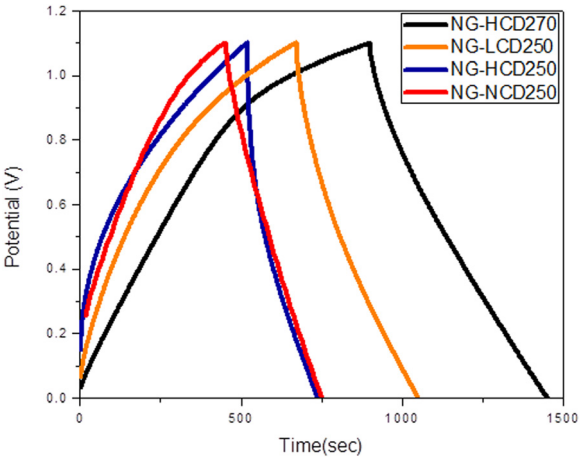

Fig. 12 Charge–discharge curves of graphitic samples.

The vertical rise of the impedance value at low frequencies indicated the good capacitive behavior. It could be noticed that the NG-HCD270 sample showed the most vertical line, followed by the NG-LCD250 sample, then the NG-HCD250 sample, and lastly the NG-NCD250 sample, with phase angles of 71°, 55°, 51°, and 47°, respectively. This reveals the improved capacitive performance by the EDLC mechanism and electrode stability, going from NG-NCD250, NG-HCD250, NG-LCD250 and eventually to NG-HCD270. On the other hand, the intercept of the curve with the real impedance axis (*x*-axis) gives the equivalent series resistance (ESR), which includes the resistance of the electrolyte, the intrinsic resistance of ACs, the contact resistance between the AC and the acetylene black particles, and the contact resistance between the electrode films and the current collectors. It was found that the ESR value decreased, going from NG-NCD250 (0.25 Ω), NG-HCD250 (0.14 Ω), NG-LCD250 (0.098 Ω), and eventually to NG-HCD270 (0.0039 Ω). Such data disclose that the NG-HCD270 electrode possessed the highest electrical conductivity and, consequently, the maximum charge-storage capacitance by the EDLC mechanism, followed by the NG-LCD250 electrode, then the NG-HCD250 electrode, and lastly the NG-NCD250 electrode. It is worth noting that the net charge-storage capacitance followed a different order through the graphitic samples (Table 3). Here, the NG-HCD270 electrode was the best, followed by the NG-LCD250 electrode, then the NG-NCD250 electrode, and lastly the NG-HCD250 electrode, which reaffirmed the contribution of the pseudocapacitive mechanism besides the EDLC mechanism in the overall charge-storage behavior of some of the graphitic samples.

Table 3 Electrochemical performances of the graphitic sample-based electrodes in two-electrode supercapacitor systems

Sample code	Specific capacitance (F g^{-1})	Energy density (W h kg^{-1})	Power density (W kg^{-1})
NG-NCD250	299	41.5	500
NG-LCD250	382	64.2	550
NG-HCD250	220	37	550
NG-HCD270	553	84.5	550.2

The EIS curve of the NG-HCD270 electrode that had the best electrochemical energy-storage performance was fitted with equivalent circuit model using Nova 2.1 software (Fig. 13(b). The obtained equivalent circuit parameters gave an R_s of 67 mΩ, W of 58.2 mM h, and C_F of 215 mF, where R_s is the Ohmic resistance derived from the electrolyte and the contact between electrode and current collector. At low frequencies, the spectrum showed an almost straight line parallel to the imaginary axis, which is related to a perfect polarized capacitive behavior described by C_F, the faradaic capacitance. In the mid-frequency region of the spectrum, a Warburg element (W) describes diffusion processes of the ions through the porous structure of the electrodes. The low value of R_s revealed the good conductivity of the measured cell. Moreover, no charge-transfer resistance (R_{ct}) was recorded, suggesting fast charge transfer in the measured cell. The large value of C_F indicates the dominant double-layer capacitance character of the NG-HCD270 electrode.

3.3. Electrochemical performance and correlation with the graphitic structural characteristics

For the NG-HCD270 sample, the remarkable electrical conductivity could be attributed to the small residual oxygenation level, good structural order, and low defect density within the sp^2-carbon lattice of the graphitic structure, in addition to, the high surface area of the nanosheets due to their extensive exfoliation and large lateral dimensions. Since CTAB is an organic material, the low density of capped CTAB molecules on the graphitic structure surface of NG-HCD270 also contributed to the high electrical conductivity of the sample. Therefore, the outstanding charge-storage capacitance by the EDLC mechanism manifested the electrochemical performance of the two-electrode supercapacitor system based on NG-HCD270. Meanwhile, there was trivial charge-storage capacitance contributed by the pseudocapacitive behavior due to the low total doped-N level and the pyrrolic-N configuration.

For the NG-LCD250 sample, despite the considerable residual oxygenation level of the graphitic structure and the relatively limited surface area of its nano-architecture due to the medial degree of nanosheets' exfoliation and its spherical morphology, the significant N-doping level, good structural order, and small density of surface-capped CTAB molecules within the graphitic structure had a profound positive effect on the charge-storage capacitive performance of the sample. Thus, the latter three graphitic structural characteristics prompted fast electron transfer and, consequently, good electrical conductivity through the sp^2-carbon network, which enhanced the capacitance occurring by the EDLC mechanism. Additionally, the doped pyridinic NO_x and pyrrolic N species within the graphitic structure induced significant charge storage by the pseudocapacitive behavior. Therefore, the good net charge-storage capacitance by the EDLC and pseudocapacitance mechanisms led to distinguished electrochemical performance of the two-electrode supercapacitor system based on NG-LCD250.

For the NG-NCD250 sample, the significant residual oxygenation level, extensive structural disorder, and small surface area, owing to the prevalent nanosheets' agglomeration and spherical architecture of the graphitic structure, were the main

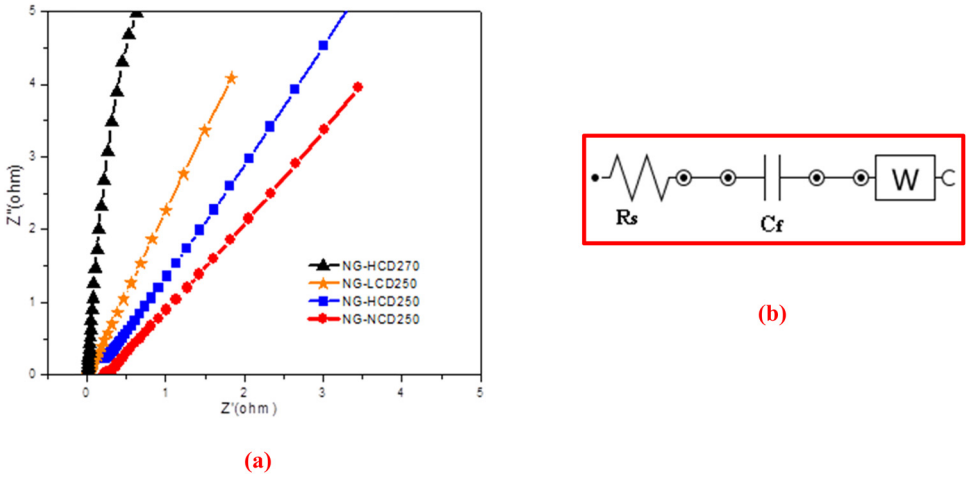

Fig. 13 (a) Nyquist plots for graphitic samples. (b) Equivalent circuit fitting of the EIS spectrum of the NG-HCD270-based electrode.

structural features considerably limiting electron transfer and, consequently, the electrical conductivity through the sp^2-carbon network of this sample. Thus, the NG-NCD250 sample had the lowest electrical conductivity, as evidenced from the ESR values, among the four graphitic samples, leading to major damping of the charge-storage capacitance by the EDLC mechanism. However, the NG-NCD250 sample had the highest N-doping level, with a considerable pyrrolic N content, among the four graphitic samples, which relatively enhanced the charge storage occurring by the pseudocapacitance mechanism. This positively contributed to the net charge-storage capacitance of the NG-NCD250 sample, causing its value not to be the minimum among the four graphitic samples.

For the NG-HCD250 sample, based on the ESR values, it showed the second lowest electrical conductivity after the NG-NCD250 sample, despite its small residual oxygenation level and reasonably extended surface area due to the good nanosheets exfoliation of the graphitic structure. The limited electron transfer and, consequently, electrical conductivity through the sp^2-carbon network of this sample could be attributed to the high density of capping CTAB molecules on its graphitic structure surface. This is because CTAB is an organic material with significantly lower electrical conductivity compared to graphene, thus hindering electron transfer throughout the sp^2-carbon network of the NG-HCD250 sample. In addition, the intensive interfacial interactions between the high concentration of CTAB molecules and the sp^2-carbon network considerably disturb the structural order within the graphitic structure of the NG-HCD250 sample, which also hinders electron transfer through this sample. The limited electrical conductivity of the NG-HCD250 sample led to a major damping of the charge-storage capacitance by the EDLC mechanism. Meanwhile, the low N-doping level within the NG-HCD250 sample, which was almost one-third that of the NG-NCD250 sample as evidenced from the N/C atomic ratio data, yielded quite a small charge-storage capacitance by the pseudocapacitance mechanism. Therefore, the net charge-storage capacitance of the NG-HCD250 sample by the EDLC and pseudocapacitance mechanisms was the minimum among the four graphitic samples.

The precedent discussion highlights the crucial role of the graphitic structural character in tuning the electrochemical performance of N-doped 2D graphene derivatives. It specifically reveals the competitive effects of the graphitic structural parameters on the energy-storage capacitive performance of symmetric two-electrode supercapacitor systems based on the investigated graphitic samples, as clearly summarized in the graphical abstract of this research article.

Overall, the NG-HCD270 graphitic sample-based electrode showed the highest energy-storage capacitive performance in two-electrode supercapacitor systems, with a remarkable specific capacitance of 553 F g^{-1}, energy density of 84.5 W h kg^{-1}, and power density of 550.2 W kg^{-1}. Further electrochemical measurements were conducted on this graphitic sample for more deeply evaluating its electrochemical energy-storage performance as an electrode material for supercapacitors.

The rate capability performance of the NG-HCD270 electrode in a two-electrode supercapacitor system was thus investigated. The CV curves at varied scan rates of 5–100 mV s^{-1} and the GCD curves at various current densities ranging from 1 to 10 A g^{-1} are demonstrated in Fig. 14(a) and (b), respectively. The CV curves preserved the quasi-rectangular shape from a low scan rate of 5 mV s^{-1} to a very high scan rate of 100 mV s^{-1} (Fig. 14(a)), indicating the good supercapacitive rate performance was mainly due to the EDLC mechanism. In addition, the current densities and consequently the integrated areas of the CV curves increased with increasing the scan rate, which may be attributed to the formation of a more efficient electrical double layer and faster charge-transfer rate and propagation within the NG-HCD270 electrode due to its high electrical conductivity.[39] All the GCD curves at different current densities (Fig. 14(b)) display good linear potential-time profiles, demonstrating the good capacitance performance of this electrode. The specific capacitance, calculated from the GCD curves, decreases with increasing current density, as shown in Fig. 14(c). The capacitance value of the NG-HCD270 electrode decreases from 553 F g^{-1} at 1 A g^{-1} to 325, 247 and 185 F g^{-1} at 3, 7 and 10 A g^{-1}, respectively. Thus, the capacitance retains 59%, 45% and 33.5 of its initial value at a large current densities of

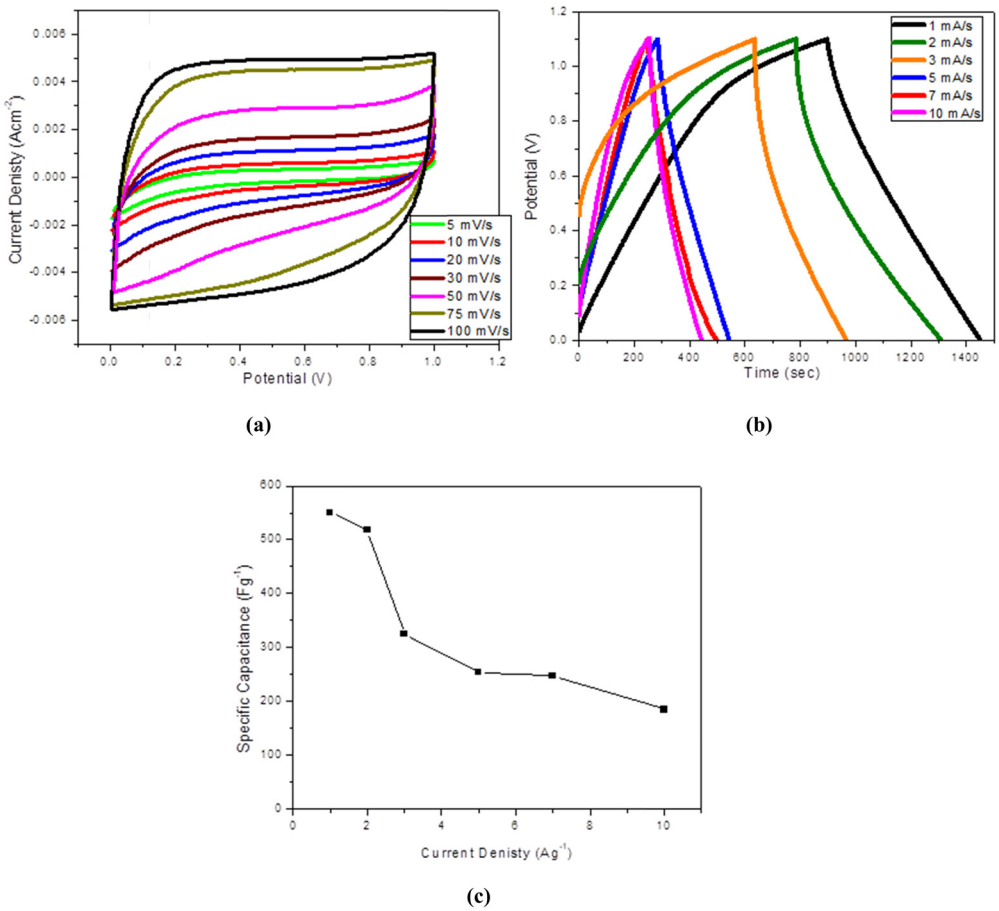

Fig. 14 Electrochemical rate capability performance of the NG-HCD270 electrode. (a) CV curves at different scan rates from 5 to 100 mV s^{-1}, (b) GCD curves at various current densities of 1–10 A g^{-1}, and (c) specific capacitance as a function of current density.

3 A g^{-1}, 7 A g^{-1} and 10 A g^{-1} respectively, indicating a good rate capability of the NG-HCD270 electrode compared to other 2D graphene derivatives reported in the literature.[39–41]

The cycling stability experiment showed that the NG-HCD270 electrode could retain 88.5% of its specific capacitance over 5000 charge–discharge cycles (Fig. 15), revealing that it had good reversibility and stability as an electrode material in supercapacitors.

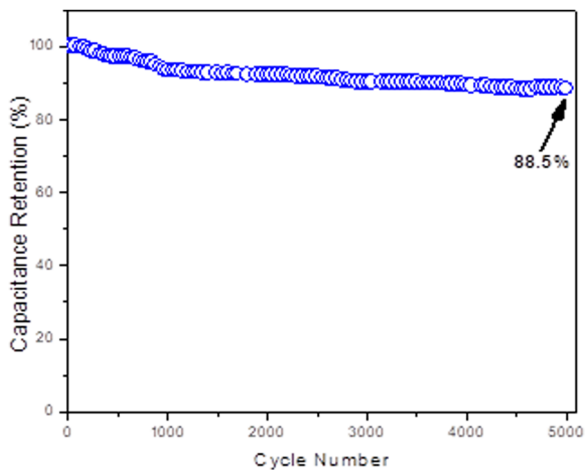

Fig. 15 Cycling stability measurements of the NG-HCD270 supercapacitor electrode.

Accordingly, the NG-HCD270 graphitic sample is considered a promising ecofriendly supercapacitor electrode material that can be produced by a novel, facile, ecofriendly, economical, and scalable production method. The electrochemical energy-storage performance of the NG-HCD270-based electrode in a symmetric two-electrode supercapacitor system was compared to those reported in the literature for graphene-like nanosheets-based electrodes in symmetric two-electrode supercapacitor systems synthesized by conventional but toxic technologies for evaluation purposes. The comparison data are reported in Table 4.

Table 4 shows that the electrochemical energy-storage performance of the NG-HCD270-based electrode demonstrated a superior specific capacitance, outstanding energy-storage density, and good cycling stability in comparison with the previously investigated graphene-like nanosheets-based electrodes that have been synthesized by the conventional toxic technologies, in symmetric two-electrode supercapacitor systems. It could be noticed that just a few previous research studies reported somewhat higher energy-storage density values, where the working potential window was as high as 3 V, than the

Table 4 Comparison of the electrochemical energy-storage performances of graphene-like nanosheet-based electrodes in symmetric two-electrode supercapacitor systems

No.	Synthesis method	Electrolyte	Specific capacitance (F g^{-1})	Energy density (W h kg^{-1})	Capacitance retention (%)	Research work
	Hydrothermal treatment of glucose	Aqueous	553	84.5	88.5% up to 5000 cycles	Present study
1.	Synthesis of porous N-doped graphene (PNG) proceeded as follows: Synthesis of GO sheets *via* the modified Hummers' method Thermal annealing of GO and urea in a tube furnace at 300 °C for 3 h and then at 800 °C for 2 h, under an N_2 atmosphere	Ionic liquid	214	***164***	89% up to 4000 cycles	39
2.	Synthesis of N-doped reduced graphene oxide (N-RGO) proceeded as follows: Synthesis of GO sheets *via* the modified Hummers' method N-RGO was then obtained *via* the reduction of GO by glycine	Aqueous	296	***128***	96.5% up to 10 000 cycles	40
3.	Graphene was commercially purchased from the Six Element (Changzhou) Materials Technology Co, Ltd	Aqueous	381.2	33.88	68.5% up to 250 cycles	41
4.	Synthesis of reduced graphene oxide (RGO) proceeded as follows: Synthesis of GO sheets *via* the modified Hummers' method RGO was then obtained *via* the reduction of GO by hydrazine hydrate	Aqueous	135	—	—	42
5.	RGO synthesis proceeded as follows: Synthesis of GO sheet *via* the modified Hummers' method Gas-based hydrazine reduction	Aqueous	205	28.5	90% up to 1200 cycles	43
6.	Synthesis of graphene *via* ultrasonic exfoliation of graphite powder in an aqueous medium using 1-pyrenecarboxylic acid (PCA)	Aqueous	120	9.2	—	44
7.	Synthesis of organoamine-modified RGO through a one-step solvothermal process of graphene oxide (GO) and *N*,*N*-dimethylformamide (DMF) at 180 °C	Aqueous	193.5	11.35	74% up to 5000 cycles	45
8.	Synthesis of N-doped graphene (NG) through a one-step solvothermal process of graphene oxide (GO) and o-phenylenediamine	Aqueous	301	—	97% up to 4000 cycles	46
9.	Synthesis of N-RGO proceeded as follows: Synthesis of GO sheets *via* the modified Hummers' method N-RGO was then obtained *via* the reduction of GO by sodium borohydride	Ionic liquid	249	34.5	—	47
10.	Synthesis of sulfurized RGO proceeded as follows: Synthesis of GO sheets *via* the modified Hummers' method Sulfurized RGO was then obtained by annealing GO powder in the H_2S atmosphere at 500 °C for 2 h	Ionic liquid	150	***124***	95% up to 20 000 cycles	48
11.	Synthesis of 1-butyl-3 methylimidazolium tetrafluoroborate ([BMIM][BF4])-modified RGO (f-RGO) proceeded as follows: Synthesis of GO sheets *via* the modified Hummers' method Solvothermal process of GO and ([BMIM][BF4]) at 150 °C for 5 h	Ionic liquid	242	***92***	90% up to 12 000 cycles	49

values obtained in the present research. Such data are highlighted as bold and italic format in Table 4.

The energy-storage capacitive performance of NG-HCD270 may be further improved in forthcoming research through hybridization with metal oxides or conductive polymers, generating composite supercapacitor electrodes. Also, a higher working potential (voltage) window may be achieved by replacement of the aqueous electrolyte with an ionic liquid one[39,48,49] and/or applying the recent strategy of mass-balancing between the positive and negative electrodes with different electrodes' masses,[50] which should effectively enhance the energy-storage capacitive performance. So, NG-HCD270-based composites may emerge as a notable ecofriendly and cost-effective electrode material for high-performance supercapacitor devices, which could benefit the further substantial development of the electrical energy-storage industry at competitive costs.

4. Conclusions

In summary, the present study reports the electrochemical energy-storage performance of symmetric two-electrode supercapacitor systems based on electrodes made from ecofriendly N-doped 2D graphene-like derivatives, which were synthesized employing a novel, facile, ecofriendly, economical, and scalable technique. Ecofriendly N-2D GDs with various graphitic structural features were produced through a single-step hydrothermal treatment of glucose in the presence of traces of CTAB and ammonia reagents, under varying hydrothermal process temperatures and CTAB doses. The electrochemical energy-storage performance was found to be strongly dependent on the oxidation level, doped-N content and configurations, graphitic structural order and defect density, nanosheets' degree of exfoliation and lateral dimensions, and density of graphitic surface-capping by CTAB within the sp^2-carbon network of the N-2D GDs-based electrodes. Importantly, the study revealed that doping pyridinic-oxide N (NO_x) and pyrrolic N at a high total N-doping level within the graphitic structure induced a significant charge storage by the pseudocapacitive behavior, besides the EDLC mechanism. Also noteworthy was the distinctive competitive effects of the graphitic structural parameters on the energy-storage capacitive performance. Thus, the residual oxygenation level became lower, which had an improving positive effect on the charge-storage capacitance in the following order for the graphitic samples: NG-NCD250 > NG-LCD250 > NG-HCD250 ≫ NG-HCD270 (lowest and the best effect). Conversely, as the N-doing content increased, it had an improving positive effect on the charge-storage capacitance in the following order for the graphitic samples; NG-HCD270 ≈ NG-HCD250 ≪ NG-LCD250 ≪ NG-NCD250 (highest and the best effect). Overall, the study highlights the crucial role of the graphitic structural character in tuning the electrochemical energy-storage performance of symmetric two-electrode supercapacitor devices based on N-2D GDs, and puts forward the NG-HCD270 graphitic sample as an advanced ecofriendly and economical supercapacitor electrode material, compared to other graphene-like nanosheets reported in the literature. This work contributes to the prominent progress of electrical energy-storage technology and, consequently, electrical power production from renewable energy sources, at competitive costs.

Author contributions

Marwa A. A. Mohamed: Propose the research idea and design the outline and the sequence of the research plan. Perform the synthesis and all the nanostructure characterizations of the investigated nitrogen-doped 2D graphene-like derivatives. Mainly, analyze and discuss the graphitic nanostructure and electrochemical results. Write the whole manuscript. Review, edit and put the manuscript in its final version for publication. Marwa Adel: Perform the deconvolution of Raman spectra and share in the analysis and discussion of its results. Jehan El Nady: Prepare the electrodes and perform all the electrochemical measurements. Plot all the electrochemical results' figures and make their mathematical calculations. Share in the analysis and discussion of the electrochemical results.

Data availability

Important and effective data generated or analyzed during this study are included in this submitted manuscript and its ESI.† Any additional clarifying data are available upon request.

Conflicts of interest

There are no conflicts of interest to declare.

Acknowledgements

Authors acknowledge the financial support for this research by the Egyptian funding agency, Science, Technology and Innovation Funding Authority (STDF), under a project (ID: 25626) entitled ''Supercapacitors based on Graphene and Graphene/Metal Oxide Hybrid Nanocomposites for Electrochemical Energy Storage. The authors also deeply appreciate Mr Amr Gamal, Dr Marwa Ramadan, Eng. Nagy Wadiaa and Eng. Hossam Awad, Central Lab. Engineers at SRTA City, for their kind assistance in performing the FTIR, Raman, SEM and HR-TEM, analyses, respectively.

References

1 S. S. Al-Juboori, Green Energy-An Introduction, in *Energy Science and Technology: Opportunities and Challenges*, ed. R. Prasad, S. Sivakumar and U. Ch. Sharma, Studium Press LLC, USA, 1st edn, 2015, pp. 316–340.
2 T. Z. Ang, M. Salem, M. Kamarol, H. S. Das, M. A. Nazari and N. Prabaharan, A comprehensive study of renewable energy sources: Classifications, challenges and suggestions, *Energy*

Strategy Rev., 2022, **43**, 100939, DOI: 10.1016/j.esr.2022.100939.

3 A. Burke, Ultracapacitors: why, how, and where is the technology, *J. Power Sources*, 2000, **91**(1), 37–50, DOI: 10.1016/S0378-7753(00)00485-7.

4 W. Yang, *et al.*, Graphene in Supercapacitor Applications, *Curr. Opin. Colloid Interface Sci.*, 2015, **20**(5–6), 416–428, DOI: 10.1016/j.cocis.2015.10.009.

5 G. Yu, X. Xie, L. Pan, Z. Bao and Y. Cui, Hybrid nanostructured materials for high-performance electrochemical capacitors, *Nano Energy*, 2013, **2**(2), 213–234, DOI: 10.1016/j.nanoen.2012.10.006.

6 Z. Li, Z. Zhou, G. Yun, K. Shi, X. Lv and B. Yang, High-performance solid-state supercapacitors based on graphene-ZnO hybrid nanocomposites, *Nanoscale Res. Lett.*, 2013, **8**(1), 473, DOI: 10.1186/1556-276X-8-473.

7 M. A. A. Mohamed, M. Adel and A. M. Abd El-Aziz, Recent trends in two-dimensional graphene derivatives-based composites: Review on synthesis, properties and applications, *J. Compos. Mater.*, 2023, **57**(27), 4327–4364, DOI: 10.1177/00219983231191271.

8 M. A. A. Mohamed, F. Carrasco-Marín, N. A. Elessawy and H. A. F. Hamad, Glucose-Derived N-Doped Graphitic Carbon: Facile One-Pot Graphitic Structure-Controlled Chemical Synthesis with Comprehensive Insight into the Controlling Mechanisms, *ChemistrySelect*, 2020, **5**(46), 14685–14702, DOI: 10.1002/slct.202003014.

9 V. V. Strelko, Role of carbon matrix heteroatoms at synthesis of carbons for catalysis and energy applications, *J. Energy Chem.*, 2013, **22**(2), 174–182, DOI: 10.1016/S2095-4956(13)60023-6.

10 L. L. Zhang, *et al.*, Nitrogen doping of graphene and its effect on quantum capacitance, and a new insight on the enhanced capacitance of N-doped carbon, *Energy Environ. Sci.*, 2012, **5**(11), 9618–9625, DOI: 10.1039/C2EE23442D.

11 T. Kwon, H. Nishihara, H. Itoi, Q.-H. Yang and T. Kyotani, Enhancement Mechanism of Electrochemical Capacitance in Nitrogen-/Boron-Doped Carbons with Uniform Straight Nanochannels, *Langmuir*, 2009, **25**(19), 11961–11968, DOI: 10.1021/la901318d.

12 Y.-H. Lee, K.-H. Chang and C.-C. Hu, Differentiate the pseudocapacitance and double-layer capacitance contributions for nitrogen-doped reduced graphene oxide in acidic and alkaline electrolytes, *J. Power Sources*, 2013, **227**, 300–308, DOI: 10.1016/j.jpowsour.2012.11.026.

13 E. Frackowiak, G. Lota, J. Machnikowski, C. Vix-Guterl and F. Béguin, Optimisation of supercapacitors using carbons with controlled nanotexture and nitrogen content, *Electrochim. Acta*, 2006, **51**(11), 2209–2214, DOI: 10.1016/j.electacta.2005.04.080.

14 A. Kausar, *et al.*, Green-Synthesized Graphene for Supercapacitors—Modern Perspectives, *J. Compos. Sci.*, 2023, **7**(3), 108, DOI: 10.3390/jcs7030108.

15 M. A. A. Mohamed, A. M. Abd El-Aziz and M. Adel, in Advances in green production of two-dimensional graphene-derivatives-based polymer composites with overview on their physicochemical characteristics and applications prospects, *Green Composites Manufacturing*, ed. G. Singh, R. P. Singh, N. Sharma and J. P. Davim, De Gruyter, 2024, ch. 9, pp. 199–256. , DOI: 10.1515/9783111067346-009.

16 M. Adel, O. El-Shazly, E. F. El-Wahidy, A. El-Maghraby and M. A. A. Mohamed, Eco-friendly produced lightweight structural graphene/polyamide 12 nanocomposite: Mechanical performance and the controlling microstructural mechanisms, *Polym. Eng. Sci.*, 2018, **58**(7), 1201–1212, DOI: 10.1002/pen.24683.

17 M. A. A. Mohamed, N. A. Elessawy, F. Carrasco-Marín and H. A. F. Hamad, A novel one-pot facile economic approach for the mass synthesis of exfoliated multilayered nitrogen-doped graphene-like nanosheets: New insights into the mechanistic study, *Phys. Chem. Chem. Phys.*, 2019, **21**(25), 13611–13622, DOI: 10.1039/c9cp01418g.

18 A. Allagui, *et al.*, Review of fractional-order electrical characterization of supercapacitors, *J. Power Sources*, 2018, **400**, 457–467, DOI: 10.1016/j.jpowsour.2018.08.047.

19 K. Krishnamoorthy, G.-S. Kim and S. J. Kim, Graphene nanosheets: Ultrasound assisted synthesis and characterization, *Ultrason. Sonochem.*, 2013, **20**(2), 644–649, DOI: 10.1016/j.ultsonch.2012.09.007.

20 M. Adel, A. El-Maghraby, O. El-Shazly, E. W. F. El-Wahidy and M. A. A. Mohamed, Synthesis of few-layer graphene-like nanosheets from glucose: New facile approach for graphene-like nanosheets large-scale production, *J. Mater. Res.*, 2016, **31**(4), 455–467, DOI: 10.1557/jmr.2016.25.

21 T. Kuila, P. Khanra, N. H. Kim, S. K. Choi, H. J. Yun and J. H. Lee, One-step electrochemical synthesis of 6-amino-4-hydroxy-2-naphthalene- sulfonic acid functionalized graphene for green energy storage electrode materials, *Nanotechnology*, 2013, **24**, 36, DOI: 10.1088/0957-4484/24/36/365706.

22 Y. J. Yang and W. Li, CTAB functionalized graphene oxide/multiwalled carbon nanotube composite modified electrode for the simultaneous determination of sunset yellow and tartrazine, *Russ. J. Electrochem.*, 2015, **51**(3), 218–226, DOI: 10.1134/S1023193515030118.

23 H. R. de Barros, *et al.*, Surface interactions of gold nanorods and polysaccharides: From clusters to individual nanoparticles, *Carbohydr. Polym.*, 2016, **152**, 479–486, DOI: 10.1016/j.carbpol.2016.07.018.

24 X. Z. Tang, *et al.*, Enhanced thermal stability in graphene oxide covalently functionalized with 2-amino-4,6-didodecylamino-1,3,5-triazine, *Carbon*, 2011, **49**(4), 1258–1265, DOI: 10.1016/j.carbon.2010.11.044.

25 W. Yang, H. Gao, Y. Zhao, K. Bi and X. Li, Facile preparation of nitrogen-doped graphene sponge as a highly efficient oil absorption material, *Mater. Lett.*, 2016, **178**, 95–99, DOI: 10.1016/j.matlet.2016.04.131.

26 D. Deng, *et al.*, Toward N-Doped Graphene *via* Solvothermal Synthesis, *Chem. Mater.*, 2011, **23**(5), 1188–1193, DOI: 10.1021/cm102666r.

27 D. Gu, Y. Zhou, R. Ma, F. Wang, Q. Liu and J. Wang, Facile Synthesis of N-Doped Graphene-Like Carbon Nanoflakes as

Efficient and Stable Electrocatalysts for the Oxygen Reduction Reaction, *Nano-Micro Lett.*, 2018, **10**(2), 1–12, DOI: 10.1007/s40820-017-0181-1.

28 Y. Dai, *et al.*, Versatile graphene quantum dots with tunable nitrogen doping, *Part. Part. Syst. Charact.*, 2014, **31**(5), 597–604, DOI: 10.1002/ppsc.201300268.

29 S. Zhuang, E. S. Lee, L. Lei, B. B. Nunna, L. Kuang and W. Zhang, Synthesis of nitrogen-doped graphene catalyst by high-energy wet ball milling for electrochemical systems, *Int. J. Energy Res.*, 2016, **40**(15), 2136–2149, DOI: 10.1002/er.3595.

30 K. Krishnamoorthy, M. Veerapandian, R. Mohan and S. J. Kim, Investigation of Raman and photoluminescence studies of reduced graphene oxide sheets, *Appl. Phys. A: Mater. Sci. Process.*, 2012, **106**(3), 501–506, DOI: 10.1007/s00339-011-6720-6.

31 A. V. Ramya, A. N. Mohan and B. Manoj, Wrinkled graphene: Synthesis and characterization of few layer graphene-like nanocarbons from kerosene, *Mater. Sci. Pol.*, 2016, **34**(2), 330–336, DOI: 10.1515/msp-2016-0061.

32 A. V. Ramya, B. Manoj and A. N. Mohan, Extraction and Characterization of Wrinkled Graphene Nanolayers from Commercial Graphite, *Asian J. Chem.*, 2016, **28**(5), 1031–1034, DOI: 10.14233/ajchem.2016.19577.

33 A. Zamiranvari, E. Solati and D. Dorranian, Effect of CTAB concentration on the properties of graphene nanosheet produced by laser ablation, *Opt. Laser Technol.*, 2017, **97**, 209–218, DOI: 10.1016/j.optlastec.2017.06.024.

34 F. Tuinstra and J. L. Koenig, Raman Spectrum of Graphite, *J. Chem. Phys.*, 1970, **53**(3), 1126–1130, DOI: 10.1063/1.1674108.

35 A. Eckmann, *et al.*, Probing the Nature of Defects in Graphene by Raman Spectroscopy, *Nano Lett.*, 2012, **12**(8), 3925–3930, DOI: 10.1021/nl300901a.

36 A. N. Mohan, B. Manoj and A. V. Ramya, Probing the nature of defects of graphene like nano-carbon from amorphous materials by Raman spectroscopy, *Asian J. Chem.*, 2016, **28**(7), 1501–1504, DOI: 10.14233/ajchem.2016.19739.

37 D. Hulicova-Jurcakova, M. Seredych, G. Q. Lu and T. J. Bandosz, Combined Effect of Nitrogen- and Oxygen-Containing Functional Groups of Microporous Activated Carbon on its Electrochemical Performance in Supercapacitors, *Adv. Funct. Mater.*, 2009, **19**(3), 438–447, DOI: 10.1002/adfm.200801236.

38 V. Strelko, V. Kuts and P. Thrower, On the mechanism of possible influence of heteroatoms of nitrogen, boron and phosphorus in a carbon matrix on the catalytic activity of carbons in electron transfer reactions, *Carbon*, 2000, **38**(10), 1499–1503, DOI: 10.1016/S0008-6223(00)00121-4.

39 D. Liu, C. Fu, N. Zhang, Y. Li, H. Zhou and Y. Kuang, Porous nitrogen-doped graphene for high energy density supercapacitors in an ionic liquid electrolyte, *J. Solid State Electrochem.*, 2017, **21**(3), 759–766, DOI: 10.1007/s10008-016-3431-0.

40 S. Thareja and A. Kumar, High Electrochemical Performance of 2.5 V Aqueous Symmetric Supercapacitor Based on Nitrogen-Doped Reduced Graphene Oxide, *Energy Technol.*, 2020, **8**(5), 1–11, DOI: 10.1002/ente.201901339.

41 Y. L. Li, *et al.*, All-solid-state Flexible Supercapacitors Based on Screen-printed Graphene Electrodes, *Int. J. Electrochem. Sci.*, 2017, **12**(11), 10567–10576, DOI: 10.20964/2017.11.32.

42 M. D. Stoller, S. Park, Z. Yanwu, J. An and R. S. Ruoff, Graphene-Based ultracapacitors, *Nano Lett.*, 2008, **8**(10), 3498–3502, DOI: 10.1021/nl802558y.

43 Y. Wang, *et al.*, Supercapacitor Devices Based on Graphene Materials, *J. Phys. Chem. C*, 2009, **113**(30), 13103–13107, DOI: 10.1021/jp902214f.

44 X. An, *et al.*, Stable Aqueous Dispersions of Noncovalently Functionalized Graphene from Graphite and their Multifunctional High-Performance Applications, *Nano Lett.*, 2010, **10**(11), 4295–4301, DOI: 10.1021/nl903557p.

45 Q. Wang, *et al.*, Covalent modified reduced graphene oxide: Facile fabrication and high rate supercapacitor performances, *Electrochim. Acta*, 2021, **369**, 137700, DOI: 10.1016/j.electacta.2020.137700.

46 Y. Lu, *et al.*, Synthesis and supercapacitor performance studies of N-doped graphene materials using o-phenylenediamine as the double-N precursor, *Carbon*, 2013, **63**, 508–516, DOI: 10.1016/j.carbon.2013.07.026.

47 K. Gopalakrishnan, K. Moses, A. Govindaraj and C. N. R. Rao, Supercapacitors based on nitrogen-doped reduced graphene oxide and borocarbonitrides, *Solid State Commun.*, 2013, **175–176**, 43–50, DOI: 10.1016/j.ssc.2013.02.005.

48 J. S. Shaikh, *et al.*, Symmetric supercapacitor: Sulphurized graphene and ionic liquid, *J. Colloid Interface Sci.*, 2018, **527**, 40–48, DOI: 10.1016/j.jcis.2018.05.022.

49 S. Kumar, U. Vikrant, S. Raj, K. Sharma and G. Singh, High performance, All solid state, flexible Supercapacitor based on Ionic liquid functionalized Graphene, *Electrochim. Acta*, 2015, **157**, 245–251, DOI: 10.1016/j.electacta.2015.01.061.

50 E. Redondo, L. W. Le Fevre, R. Fields, R. Todd, A. J. Forsyth and R. A. W. Dryfe, Enhancing supercapacitor energy density by mass-balancing of graphene composite electrodes, *Electrochim. Acta*, 2020, **360**, 136957, DOI: 10.1016/j.electacta.2020.136957.